

GJ 1252b: A Hot Terrestrial Super-Earth with No Atmosphere

Ian J. M. Crossfield¹, Matej Malik² , Michelle L. Hill³ , Stephen R. Kane³ , Bradford Foley⁴ , Alex S. Polanski¹ , David Coria¹, Jonathan Brande¹ , Yanzhe Zhang¹, Katherine Wienke¹, Laura Kreidberg⁵ , Nicolas B. Cowan^{6,7} , Diana Dragomir⁸ , Varoujan Gorjian⁹ , Thomas Mikal-Evans⁵, Björn Benneke¹⁰ , Jessie L. Christiansen¹¹ , Drake Deming², and Farisa Y. Morales⁹

¹ Department of Physics and Astronomy, University of Kansas, Lawrence, KS, USA; ianc@ku.edu

² Department of Astronomy, University of Maryland, College Park, MD 20742, USA

³ Department of Earth and Planetary Sciences, University of California Riverside, 900 University Ave, Riverside, CA 92521, USA

⁴ Earth and Planets Laboratory, Carnegie Institution for Science, Washington, DC 20015, USA

⁵ Max-Planck Institut für Astronomie, Königstuhl 17, D-69117, Heidelberg, Germany

⁶ Department of Physics, McGill University, Montréal, QC H3A 2T8, Canada

⁷ Department of Earth & Planetary Sciences, McGill University, Montréal, QC H3A 2T8, Canada

⁸ Department of Physics and Astronomy, University of New Mexico, Albuquerque, NM, USA

⁹ Jet Propulsion Laboratory, California Institute of Technology, Pasadena, CA, USA

¹⁰ Département de Physique, and Institute for Research on Exoplanets, Université de Montréal, Montréal, Canada

¹¹ Caltech/IPAC-NASA Exoplanet Science Institute, Pasadena, CA 91125, USA

Received 2022 April 26; revised 2022 June 30; accepted 2022 July 11; published 2022 September 23

Abstract

In recent years, the discovery of increasing numbers of rocky, terrestrial exoplanets orbiting nearby stars has drawn increased attention to the possibility of studying these planets’ atmospheric and surface properties. This is especially true for planets orbiting M dwarfs, whose properties can best be studied with existing observatories. In particular, the mineralogical composition of these planets and the extent to which they can retain their atmospheres in the face of intense stellar irradiation both remain unresolved. Here, we report the detection of the secondary eclipse of the terrestrial exoplanet GJ 1252b, obtained via 10 eclipse observations using the Spitzer Space Telescope’s IRAC2 4.5 μm channel. We measure an eclipse depth of 149_{-32}^{+25} ppm, corresponding to a dayside brightness temperature of 1410_{-125}^{+91} K. This measurement is consistent with the prediction for a bare rock surface. Comparing the eclipse measurement to a large suite of simulated planetary spectra indicates that GJ 1252b has a surface pressure of $\lesssim 10$ bar, i.e., substantially thinner than the atmosphere of Venus. Assuming energy-limited escape, even a 100 bar atmosphere would be lost in < 1 Myr, far shorter than our gyrochronological age estimate of 3.9 ± 0.4 Gyr. The expected mass loss could be overcome by mantle outgassing, but only if the mantle’s carbon content were $> 7\%$ by mass—over two orders of magnitude greater than that found in Earth. We therefore conclude that GJ 1252b has no significant atmosphere. Model spectra with granitoid or feldspathic surface composition, but with no atmosphere, are disfavored at $> 2\sigma$. The eclipse occurs just $+1.4_{-1.0}^{+2.8}$ minutes after orbital phase 0.5, indicating $e \cos \omega = +0.0025_{-0.0018}^{+0.0049}$, consistent with a circular orbit. Tidal heating is therefore likely to be negligible with regard to GJ 1252b’s global energy budget. Finally, we also analyze additional, unpublished TESS transit photometry of GJ 1252b, which improves the precision of the transit ephemeris by a factor of 10, provides a more precise planetary radius of $1.180 \pm 0.078 R_{\oplus}$, and rules out any transit-timing variations with amplitudes $\gtrsim 1$ minute.

Unified Astronomy Thesaurus concepts: [Exoplanet surface composition \(2022\)](#); [Exoplanet atmospheric composition \(2021\)](#); [M dwarf stars \(982\)](#); [Eclipses \(442\)](#); [Transits \(1711\)](#)

Supporting material: data behind figures

1. Introduction

Rocky planets on short-period orbits are among the most common planetary bodies known to emerge from the process of star and planet formation (e.g., Fulton & Petigura 2018). Though too small to retain a primordial hydrogen envelope, such planets may produce secondary atmospheres later in their evolution. For example, in the solar system, rocky bodies exhibit a wide diversity of atmospheric surface pressures from Venus (92 bar), to Earth and Titan (~ 1 bar), to Mars (6 mbar), to Mercury and the Moon (negligible atmospheres).

The conditions under which terrestrial planets can retain sizable atmospheres under different irradiation levels, time-scales, types of host star, and planet masses, radii, and surface gravity all remain areas of active research. While an exoplanet’s atmosphere can be studied via transit and/or eclipse observations, transmission spectroscopy has so far failed to conclusively determine the properties (or absence of) any rocky planet’s atmosphere (e.g., see Wordsworth & Kreidberg 2021). To date, emission measurements have offered the best prospects for studying the properties of terrestrial exoplanets.

Secondary eclipses of several rocky planets were detected at optical wavelengths by the Kepler/K2 missions (e.g., Batalha et al. 2011; Sheets & Deming 2014; Malavolta et al. 2018). Unfortunately, such measurements often suffer from a degeneracy: optical eclipses represent a combination of



Original content from this work may be used under the terms of the [Creative Commons Attribution 4.0 licence](#). Any further distribution of this work must maintain attribution to the author(s) and the title of the work, journal citation and DOI.

reflected/scattered light and thermal emission, with no empirical way to determine the relative contributions of each.

Until now, thermal infrared radiation has been measured from only two terrestrial exoplanets: LHS 3844b (Kreidberg et al. 2019) and K2-141b (Zieba et al. 2022). Spitzer 4.5 μm observations of these planets’ eclipse and phase curves revealed no phase offset and suggested an upper limit to the atmospheric surface pressure; for example, the data set for LHS 3844b indicates $P_{\text{surf}} \lesssim 10$ bar.

In this paper, we report 4.5 μm eclipse photometry that reveals thermal emission, and similar constraints on the atmosphere, of GJ 1252b, the smallest exoplanet for which such a measurement has been made to date. The planet has an Emission Spectroscopy Metric (ESM; Kempton et al. 2018) of 17, slightly larger than that of K2-141b and a factor of two smaller than LHS 3844b. GJ 1252b was identified by the TESS project as TESS Object of Interest (TOI) 1078.01 in data from Sector 13, the last southern sector to be observed in the first year of TESS operations. Shporer et al. (2020) confirmed the planetary nature of the signal using a combination of TESS photometry and HARPS radial velocities. They reported a planet orbiting an M3V star with radius of $1.193 \pm 0.074 R_{\oplus}$, and the planet’s mass is $1.32 \pm 0.28 M_{\oplus}$ (Luque et al., in review).

In Section 2, we present our TESS and Spitzer observations and our analyses of these data. Section 3 then discusses these measurements in light of a set of models of planetary spectra, leading us to conclude that any atmosphere on GJ 1252b likely has a surface pressure of $\lesssim 10$ bar. Section 4 presents our predictions for atmospheric escape from GJ 1252b, which leads us to conclude that even an atmosphere with surface pressure >10 bar would be lost on a timescale much shorter than the system age. Finally, we close with a discussion of GJ 1252b in the context of similar measurements of other rocky exoplanets in Section 5.

2. Observations

2.1. New TESS Transit Photometry

Subsequent to the mid-2019 TESS Sector 13 photometry used to first discover GJ 1252b (Shporer et al. 2020), the system was reobserved during the TESS Sector 27 Campaign using Camera 2 from 2020 July 5 to 2020 July 30. In this section, we describe our combined analysis of both the original Sector 13 and the new Sector 27 data. By performing a global fit on data sets separated by nearly a year, we further refine the orbital and planetary properties of GJ 1252b.

We downloaded both Sectors 13 and 27 Presearch Data Conditioning (PDC) time series measurements from MAST. PDC-level data products are corrected for instrumental systematics and contamination from nearby stars. Our analysis used the `LightKurve` package (Lightkurve Collaboration et al. 2018) to perform five iterations of 3σ outlier rejection on data points above the median flux level. This removed 0.2% of data from the lightcurve. To remove any remaining flux variations, we flattened the lightcurve using a Savitzky–Golay filter (Savitzky & Golay 1964) after first masking out the transits (with one transit duration on either side) before applying the filter to ensure the transit features are not affected.

We fit the flattened lightcurve using the `exoplanet` package (Foreman-Mackey et al. 2021), which uses a Hamiltonian Monte Carlo (HMC) routine to explore the

Table 1
Planet Parameters

Parameter	Units	Value	Source
Stellar Parameters:			
R_*	R_{\odot}	0.391 ± 0.020	Shporer et al. (2020)
M_*	M_{\odot}	0.381 ± 0.019	Shporer et al. (2020)
T_{eff}	K	3458 ± 137	Shporer et al. (2020)
age	Gyr	3.9 ± 0.4	This work, derived
TESS Transit Parameters:			
T_0	BJD_{TDB}	$2458668.09748 \pm 0.00032$	This work, fit
P	d	$0.51824160 \pm 0.00000069$	This work, fit
i	deg	84.8 ± 3.2	This work, derived
R_p/R_*	...	0.0277 ± 0.0011	This work, fit
a/R_*	...	5.03 ± 0.27	This work, derived
T_{14}	hr	0.724 ± 0.013	This work, fit
b	...	0.42 ± 0.24	This work, fit
a	au	$0.00915^{+0.00015}_{-0.00015}$	This work, derived
S_{inc}	S_{\oplus}	233^{+48}_{-41}	This work, derived
R_p	R_{\oplus}	1.180 ± 0.078	This work, derived
M_p	M_{\oplus}	1.32 ± 0.28	Luque et al., in review
Spitzer Eclipse Parameters:			
T_E	BJD_{TDB}	$2458668.3575^{+0.0019}_{-0.0007}$	This work, fit
δ_{IRAC2}	ppm	149^{+25}_{-32}	This work, fit
dt	min	$+1.4^{+2.8}_{-1.0}$	This work, derived
$e \cos \omega$...	$+0.0025^{+0.0049}_{-0.0018}$	This work, derived
T_{day}	K	1410^{+91}_{-125}	This work, derived
f	...	>0.40	This work, derived
A_B	...	<0.41	This work, derived
$f(1 - A_B)$...	>0.37	This work, derived

Note. Two-sided intervals indicate 68.3% (1σ) confidence; one-sided intervals indicate 95.4% (2σ) confidence.

posterior probability distribution. Assuming a circular orbit with the period (P), time of inferior conjunction (T_0), scaled planet radius (R_p/R_*), impact parameter (b), transit duration (T_{14}), and mean flux offset (μ) as free parameters, we minimized a negative log-likelihood function. Our analysis held quadratic limb-darkening coefficients constant at $u_0 = 0.2800$ and $u_1 = 0.3683$ (values taken from Claret 2017). We used the values obtained from the minimizer as initial positions for 32 parallel chains and ran the HMC for 2000 tuning steps and 4000 sampling steps per chain. Loose Gaussian priors (much wider than the final posteriors) were placed on P (mean 0.51 days, width σ 0.05 days) and T_{conj} (mean 1668.0, width 0.1) to prevent the sampler from wandering too far astray. The final Gelman–Rubin statistics of the HMC runs were <1.01 for all parameters.

The median values and their 1σ uncertainties are listed in Table 1, and the model fit to binned TESS data is shown in Figure 1. Our results agree well with those of the original discovery paper (Shporer et al. 2020). As an independent check, we also analyzed the full, two-sector TESS data set using the transit lightcurve code described in numerous similar K2 studies (e.g., Crossfield et al. 2015, 2016), and found consistent parameters in all cases.

We analyze only the transits because the current TESS data cannot usefully constrain the planet’s eclipse depth. In the TESS bandpass, the contribution from either thermal emission (Figure 6) or reflected light (Section 3.2.1) is $\lesssim 15$ ppm, significantly smaller than our TESS transit depth precision of 61 ppm (Table 1).

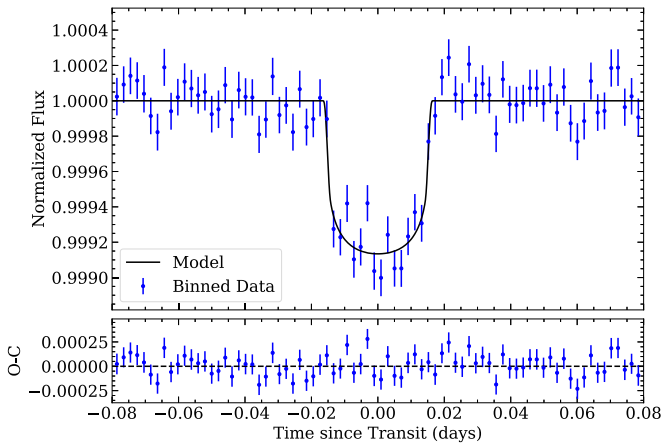


Figure 1. Folded and binned two-sector TESS lightcurve (blue points) with the median model plotted in black. Residuals (data minus model) are shown in the lower panel.

Finally, we also performed a search for transit-timing variations (TTVs) in the TESS data, again using the *exoplanet* package. If present, TTV signals could indicate the presence of undiscovered companions due to mutual gravitational interactions or orbital decay due to tidal effects. Although the S/Ns of individual transit events are quite low, we find no evidence for TTVs with amplitudes $\gtrsim 1$ minute, consistent with a lack of strongly perturbing companions. The deviation of GJ 1252b’s individually measured transit times is consistent with a linear ephemeris across both sectors of TESS data. With nearly a year separating these two sectors of TESS data, our analysis reduces the uncertainty on the period by an order of magnitude (see Table 1).

2.2. Spitzer Eclipse Photometry and Analysis

2.2.1. Eclipse Observations

Soon after the TESS project’s announcement of a planet candidate around GJ 1252, and before the planet’s confirmation by Shporer et al. (2020), we identified the planet candidate as a promising target for thermal infrared emission measurements obtained during secondary eclipse. Using preliminary information provided in the TESS alert and the TESS Input Catalog (TIC; Stassun et al. 2018), we estimated that a coordinated campaign of Spitzer eclipse observations could detect the planet’s eclipses. We therefore scheduled 10 $4.5 \mu\text{m}$ eclipse observations as part of Spitzer Program 14084 (Crossfield et al. 2018).

We observed the 10 eclipses of GJ 1252b over 10 days in 2020 January. The final observations were taken on UT 2020 January 21, less than 10 days before Spitzer was deactivated on 2020 January 30. Each eclipse observation was an identical, 2.9 hr, continuous, staring observation centered on the predicted time of secondary eclipse (i.e., orbital phase 0.5). The visits consisted of 5120 subarray frames with 2 s integrations, taken with the IRAC2 $4.5 \mu\text{m}$ camera (Fazio et al. 2004). The observations used IRAC’s peak-up mode to place the star near a well-characterized and well-behaved region of the detector, in order to minimize the effect of IRAC’s well-known intrapixel sensitivity variations. Table 2 lists the times and orbital phases of each of the 10 eclipse observations.

Table 2
Spitzer/IRAC $4.5 \mu\text{m}$ Observations

AOR	Start Date (BJD _{TDB})	Start Phase	End Phase	δ (ppm)	σ_δ (ppm)
71407360	2458868.859948	0.3917	0.6228	86	88
71407872	2458867.834249	0.4125	0.6436	101	97
71408384	2458866.277380	0.4084	0.6395	−4	88
71408640	2458864.190715	0.3819	0.6131	168	83
71408896	2458863.686588	0.4092	0.6403	44	87
71409152	2458863.163738	0.4003	0.6314	123	86
71409408	2458861.090252	0.3993	0.6304	221	83
71409664	2458860.062523	0.4162	0.6473	357	103
71409920	2458859.008577	0.3825	0.6136	307	88
71410176	2458869.902201	0.4028	0.6340	137	83

2.2.2. Eclipse Analysis

We analyzed the Spitzer photometry using Pixel-Level Decorrelation (PLD; Deming et al. 2015), which models the systematics-dominated Spitzer lightcurve as a linear combination of basis vectors derived from each pixel’s time series. Specifically, we use the formulation

$$f_{ik} = \left(\sum_{j=1}^{N+M} c_{jk} v_{ijk} \right) m_{ik}, \quad (1)$$

where f_{ik} is the modeled flux at the i th time step of the k th eclipse visit, c_{jk} is the scaling coefficient for the corresponding basis vector v_{ijk} , and m_{ik} is the purely astrophysical model of a secondary eclipse. The basis vectors v_{ijk} always include the N individual pixel time series from the k th visit (the “pixel-level” data essential to PLD) and may also include M low-order temporal trends (for which $v_{ijk} = t_{ijk}^p$ for $p = 0, 1, \dots, (M-1)$) or other systematic vectors against which the data will be decorrelated. In our analysis, we included a linear trend with time in order to remove a slow, long-term drift. We parameterized the eclipse model (m_{ik}) using the Mandel & Agol (2002) formulae for the occultation of an object with uniform surface brightness, with its only free parameters being the time of mid-eclipse T_E and the fractional eclipse depth δ .

PLD is often applied by simultaneously sampling the posterior distribution of the nuisance parameters c_{jk} as well as the astrophysical parameters of interest. In our case, this turned out to be intractable. With 10 eclipse visits, the use of $N=9$ pixels and $M=1$ (constant scaling, linear polynomial trend) would require marginalizing over 100 nuisance parameters to obtain measurements of just two astrophysical parameters, T_E and δ .

Instead, we determine T_E and δ , and their uncertainties, as follows. For each combination of these parameters, we calculate a model eclipse lightcurve and divide the observed flux F_{ik} by it. The result is

$$\frac{F_{ik}}{m_{ik}} \approx \sum_{j=1}^{N+M} c_{jk} v_{ijk} + \epsilon_{ik}, \quad (2)$$

where ϵ_{ik} represent the measurement errors. We then directly solve Equation (2) at each point for the c_{jk} using weighted linear least squares. This approach allows us to directly sample the two-dimensional (T_E, δ) plane while also accounting for the interrelationships of these astrophysical parameters on the c_{jk}

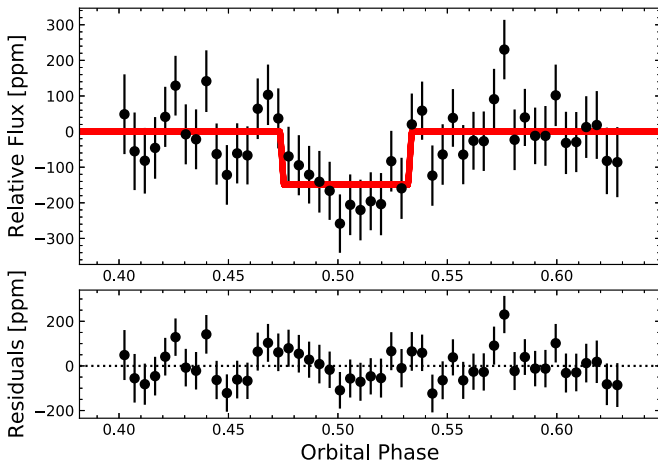


Figure 2. Spitzer 4.5 μm photometry and secondary eclipse fit (top) and residuals to the fit (bottom). The photometry is shown after detrending for systematic effects, combining the photometry from all 10 eclipse visits, and binning down to a two-minute cadence. The measured depth is 149_{-32}^{+25} ppm.

nuisance parameters. This approach is similar in some ways to the PLD analysis of Spitzer/IRAC microlensing observations (Dang et al. 2020); the main difference is that that work had more than two astrophysical parameters of interest and so used MCMC sampling instead of directly calculating a grid of likelihood values.

We set the weight of each observation equal to $1/\sigma^2$, where σ is the 68.3% central confidence interval on the dispersion of the residuals to an initial fit. Flux measurements F_{ik} are set to zero weight if they deviate by more than 5σ from the nominal model.

The resulting stacked, detrended eclipse lightcurve shown in Figure 2 shows a clear flux decrement of 149_{-32}^{+25} ppm at the expected time of eclipse. Our measured eclipse parameters are listed in Table 1, while the lightcurves for each individual visit, as well as Allan deviation plots of the residuals to each visit, are shown in the Appendix. As two checks on our measured eclipse depth, we also calculated the weighted mean of the eclipse depths from each individual visit, and we conducted a joint analysis in which the time of eclipse was held fixed to orbital phase 0.5. The weighted mean is 150 ± 28 ppm, while the fixed-time analysis yields a depth of 140_{-20}^{+35} ppm; both these values are consistent with the value obtained from our joint fit.

2.3. Stellar Age from Gyrochronology

Finally, to interpret our measurements of GJ 1252b’s thermal emission and estimate its atmospheric evolution (described below), we need to estimate a stellar age. Inferring ages for mature, field M dwarfs is notoriously challenging; one promising avenue for all but the latest M spectral subtypes is the use of gyrochronology. Using the spindown analysis of Engle & Guinan (2018) together with GJ 1252’s stellar rotation period of 64 ± 4 days (Shporer et al. 2020), we estimate GJ 1252’s age to be 3.9 ± 0.4 Gyr. This indicates that GJ 1252 is somewhat younger than LHS 3844 (7.8 ± 1.6 Gyr; Kane et al. 2020), an estimate broadly consistent with the nondetection of stellar flares during the first sector of TESS observations of GJ 1252 (Howard 2022). This result also indicates that the GJ 1252 system is somewhat younger than the 7.8 ± 1.6 Gyr LHS 3844b (Kane et al. 2020).

3. Timing, Tides, and Atmospheres

Our analysis of the Spitzer/IRAC2 4.5 μm photometry clearly detects the secondary eclipse signal, which has a depth of $\delta = 149_{-32}^{+25}$ ppm and a timing offset from orbital phase 0.5 of just $+1.4_{-1.0}^{+2.8}$ minutes (the joint posterior distribution of eclipse depth and eclipse timing is shown in the Appendix). Here, we discuss the implications of these measurements: first of the eclipse timing in Section 3.1, and then of the measured depth in Section 3.2.

3.1. Eclipse Time and Implications

The offset of the eclipse time from orbital phase 0.5 constrains the combination of orbital parameters $e \cos \omega$ (Winn 2010); for GJ 1252b, we find $e \cos \omega = +0.0025_{-0.0018}^{+0.0049}$. This result is consistent with zero at the 1.4σ level, so we do not take this measurement as evidence of an eccentric orbit. Regardless, the $e \cos \omega$ measurement further justifies the assumption of low eccentricity in the radial velocity analysis of Shporer et al. (2020). We conducted a reanalysis of their radial velocity data while incorporating this new constraint on $e \cos \omega$, finding results consistent with those of the discovery paper.

Although GJ 1252b’s orbit would quickly circularize in the absence of other perturbers, small planets orbiting M dwarfs are often found in multiplanet systems, and additional bodies in the system could cause GJ 1252b to stay on an eccentric orbit. Although no such bodies were indicated by our TTV analysis, it is still possible that tidal heating could act as an additional heat source in GJ 1252b. We estimate this heating level following the prescription of Henning et al. (2009) and assuming a Love number $k_2 = 0.3$ and tidal quality factor $Q = 10^4$, approximately appropriate for super-Earths (Miguel et al. 2011; Millholland & Laughlin 2019). Further assuming that $e = 0.0025$, we find that tidal heating should contribute only 4×10^{16} W to GJ 1252b’s total energy budget; this amount is negligible (unless tidal heating is enhanced via a significantly nonzero axial tilt; Millholland & Laughlin 2019) compared to the roughly 6×10^{19} W of starlight absorbed by the planet.

3.2. Eclipse Depth and Implications

Here, we consider the implications of our eclipse measurement on the surface and atmospheric properties of GJ 1252b. We first consider our results in the context of global energy balance in Section 3.2.2, and then in the context of a suite of one-dimensional radiative transfer models in Section 3.2.3.

3.2.1. From Eclipse Depth to Brightness Temperature

Converting an eclipse depth measurement into a brightness temperature requires an estimate of both R_p/R_* and of the stellar flux density at the relevant wavelengths. Since M dwarfs such as GJ 1252 have emergent spectra that differ considerably from simple blackbodies, appropriate stellar spectra must be used. We used the BT-Settl suite of stellar models (Allard 2014), interpolating across the model grid using the T_{eff} , $\log_{10} g$, and $[\text{Fe}/\text{H}]$ from Shporer et al. (2020). The result is that GJ 1252b’s dayside has a 4.5 μm brightness temperature of 1410_{-125}^{+91} K, considerably hotter than the equilibrium temperature of 1089 ± 69 K reported by Shporer et al. (2020).

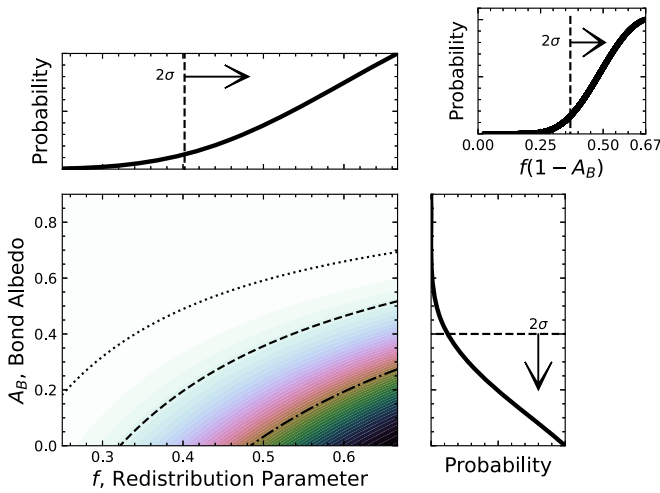


Figure 3. Joint constraints on Bond albedo and the heat redistribution parameter, assuming that GJ 1252b radiates as a blackbody at its $4.5 \mu\text{m}$ brightness temperature. More heavily shaded regions indicate higher probabilities in the main panel, with the contour lines demarcating the enclosed 1σ , 2σ , and 3σ confidence intervals. The dashed lines in the 1D posterior distribution plots show the 95.4% (2σ) confidence limit for the indicated parameter. Our measurements of GJ 1252b constrain $f > 0.40$, $A_B < 0.41$, and $f(1 - A_B) > 0.37$.

We note that reflection or scattered light contribute only $(R_p/a)^2 A_g \approx (30 \text{ ppm} \times A_g)$ to the eclipse depth, where A_g is the planet’s $4.5 \mu\text{m}$ broadband geometric albedo. With $A_g < 0.5$ expected for most typical minerals (Mansfield et al. 2019) and < 0.1 for lava or volcanic glasses (Essack et al. 2020; Modirrousta-Galian et al. 2021), the contribution of surface reflection to our measurement is $< 15 \text{ ppm}$, i.e., smaller than our Spitzer (or TESS) measurement precision.

3.2.2. Energy Balance and Atmospheric Circulation

One phenomenological framework for interpreting single-band secondary eclipse measurements is to assume the planet radiates as a blackbody at the measured brightness temperature, then to use the measurement to constrain some combination of day-to-night heat redistribution parameter f and Bond Albedo A_B (e.g., Seager 2010). In particular, the combination $f(1 - A_B)$ directly determines the planet’s dayside equilibrium temperature via

$$T_{\text{eq}} = T_{\text{eff}} \sqrt{\frac{R_*}{a}} (f[1 - A_B])^{1/4}. \quad (3)$$

In this formulation, the limiting values of f are $\frac{2}{3}$, indicating no heat redistribution (e.g., consistent with no atmosphere) and $\frac{1}{4}$, indicating uniform heat redistribution around the planet. Figure 3 shows our joint constraints on f and A_B , assuming flat priors on both quantities and the system parameters listed in Table 1. In all cases, the most likely values are the ones that give the highest dayside T_{eq} , i.e., $f = \frac{2}{3}$ and $A_B = 0$. We set upper limits (at 95.4%, or 2σ confidence) of a low albedo of $A_B < 0.41$; a high redistribution parameter of $f > 0.40$; and a high combination of the two, $f(1 - A_B) > 0.37$.

3.2.3. One-dimensional Atmosphere Models

Finally, we also present a large suite of atmospheric models and spectra of GJ 1252b. These models are all available as

machine-readable supplements to this paper. Our models and spectra are generated using the open-source, 1D radiative transfer code HELIOS (Malik et al. 2017, 2019a, 2019b), which simulates the planet in radiative-convective equilibrium and also provides the functionality to include the radiative effects of a non-gray surface on both the atmosphere and the planetary spectrum (see E. A. Whittaker et al. 2022, in preparation).

In HELIOS, the temperature profile and surface temperature are obtained using the k-distribution method, with 420 wavelength bins ($0.245\text{--}10^5 \mu\text{m}$). Then, starting from the equilibrium temperature profile, the planetary spectrum is calculated using opacity sampling with a resolution of $R = 4000$. Convectively unstable atmospheric layers are corrected using convective adjustment. We model dayside-averaged conditions and use the scaling theory of Koll (2022) to estimate the amount of heat transported from the dayside to the nightside of the planet. In the bare-rock case, the heat redistribution parameter (f in Equation (3)) is set to $2/3$, equivalent to no horizontal heat transport (Burrows et al. 2008; Hansen 2008).

Gaseous opacities are calculated with HELIOS-K (Grimm & Heng 2015; Grimm et al. 2021), including O_2 (Gordon et al. 2017), N_2 (Gordon et al. 2022), H_2O (Polyansky et al. 2018), CO (Li et al. 2015), CO_2 (Rothman et al. 2010), CH_4 (Yurchenko et al. 2017), and SO_2 (Underwood et al. 2016). All opacities are calculated on a fixed grid with a resolution of 0.01 cm^{-1} , assuming a Voigt profile truncated at 100 cm^{-1} from line center. For H_2O , CH_4 , and SO_2 the default pressure broadening coefficients provided by the Exomol database¹² are included. For O_2 , N_2 , CO , and CO_2 , the HITRAN broadening formalism for self-broadening is used. Further included are collision-induced absorption (CIA) by $\text{O}_2\text{--O}_2$, $\text{O}_2\text{--CO}_2$, $\text{CO}_2\text{--CO}_2$, $\text{N}_2\text{--N}_2$, and $\text{N}_2\text{--CH}_4$ pairs (Richard et al. 2012) and Rayleigh scattering of H_2O , O_2 , N_2 , CO_2 , and CO (Cox 2000; Snee & Ubachs 2005; Wagner & Kretschmar 2008; Thalman et al. 2014).

To model the radiative effects of the surface, we use the geometric albedo spectra from Hu et al. (2012). For the bare-rock scenario, HELIOS again iterates the surface temperature until the surface is in radiative equilibrium, i.e., the downward stellar radiation equals the reflected plus emitted radiation at the surface boundary. This takes the non-gray surface albedo into account across the range of $0.3\text{--}25 \mu\text{m}$, thus correctly treating both the stellar flux absorption and reflection as well as the planetary emission.

When modeling the planetary envelope, we include the main infrared absorbers that may be plausibly found in secondary atmospheres— H_2O , CO_2 , CO , CH_4 , and SO_2 (see, e.g., Gillmann et al. 2022)—and vary their mixing ratios between 1 ppm and 1% (Gaillard & Scaillet 2014). As background gas, we use O_2 or N_2 (Wordsworth & Pierrehumbert 2014; Luger & Barnes 2015; Schaefer et al. 2016; Lammer et al. 2019). As limiting cases, we also approximate post-water-runaway, Venus-like, and carbon-rich (elemental C/O ~ 1) atmospheres by adding pure H_2O , CO_2 , and CO scenarios (Madhusudhan 2012; Kane et al. 2014; Goldblatt 2015). Specifically, the full range of our models included either CO or CH_4 in an N_2 -dominated atmosphere; CO_2 , SO_2 , or H_2O in an O_2 -dominated atmosphere; and atmospheres of pure CO_2 ,

¹² <https://exomol.com/data/molecules/>

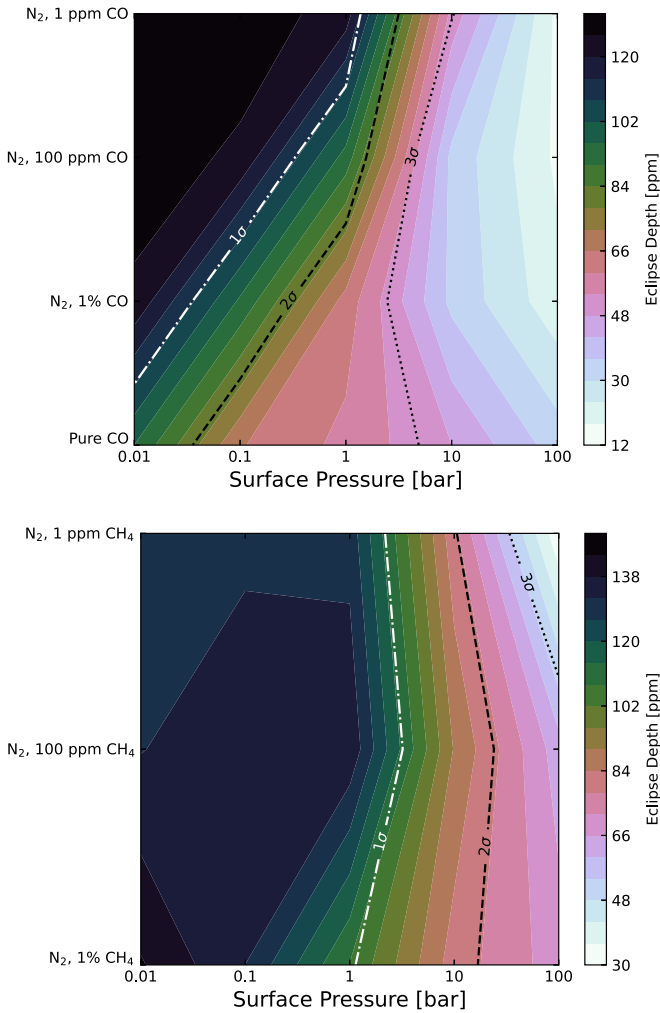


Figure 4. Predicted IRAC2 $4.5 \mu\text{m}$ eclipse depths (colored shading) from our suite of atmospheric models for atmospheres dominated by N_2 ; each model has a single dominant, active IR absorber of either CO (top) or CH_4 (bottom). The contour lines indicate the level of agreement with our eclipse measurement of 149^{+25}_{-32} , with darker regions being more consistent with our data. Thick atmospheres with $P_{\text{surf}} \gtrsim 10$ bar are disfavored by all modeled mixing ratios. (The data used to create this figure are available.)

SO_2 , or H_2O . These models are not intended to be exhaustive (nor may they all be chemically stable on geological timescales); our goal is to explore a representative range of atmospheres without overinterpreting our single-channel measurement.

For each model emission spectrum, we calculated the eclipse depth that would be measured in the $4.5 \mu\text{m}$ IRAC2 bandpass. Figures 4 and 5 compare our measured $4.5 \mu\text{m}$ eclipse depths to the predictions of our atmospheric models dominated by N_2 and O_2 , respectively. For the N_2 -dominated models, Figure 4 shows that the only models consistent with our eclipse measurement at 2σ or better have $P_{\text{surf}} \lesssim 1$ bar (for CO as the active IR absorber) and $\lesssim 10$ bar (for CH_4). Similarly, Figure 5 shows that the O_2 -dominated models consistent with our measurement at 2σ have $P_{\text{surf}} \lesssim 1$ bar (for CO_2) and $\lesssim 10$ bar (for SO_2 or H_2O).

We also find that models lacking any atmosphere are also consistent with our eclipse measurement. Figure 6 shows that, while only the gray and metal-rich bare-rock models are

consistent with our measurement at $<1\sigma$, models with an oxidized Fe, basaltic, and ultramafic surface composition are all consistent with our eclipse at $<2\sigma$. Models with a feldspathic or granitoid surface composition are inconsistent with the data at $>2\sigma$. However, we note that the substellar region of GJ 1252b is likely hot enough for such materials to melt. Although our atmosphere-free models may not be strictly accurate for this planet’s surface, we leave more detailed models involving both solid and melted regions for future study.

4. Atmospheric Evolution and Escape

Zahnle & Catling (2017) postulate a “cosmic shoreline” in which the ability of a body to retain an atmosphere depends on some combination of its escape velocity v_{esc} , bolometric irradiation S , and extreme UV (XUV) irradiation. Given its irradiation and $v_{\text{esc}} = 5.4 \pm 0.8 \text{ m s}^{-1}$, GJ 1252b would lie well into the atmosphere-free zone—but then so would 55 Cnc e, where infrared measurements seem to indicate the presence of an atmosphere (Demory et al. 2016a, 2016b; Angelo & Hu 2017; Hammond & Pierrehumbert 2017; Tamburo et al. 2018). Thus, the cosmic shoreline may not apply universally to smaller exoplanets irradiated so much more intensely than anything in the solar system.

The evolution of a planetary atmosphere into its end-state depends on the mantle’s cooling rate, regions of oxidization, and potential sinks for these volatiles (e.g., Gillmann et al. 2022). For example, N_2 is interesting because there are relatively few sinks and so, despite N_2 being a relatively small amount of the Earth’s total volatile inventory, it dominates the present atmosphere. Another interesting species to think about is SO_2 : the sulfur cycle on Venus is an important component of its overall atmospheric chemistry, and so SO_2 is a significant component of volcanic outgassing on Venus (Esposito 1984; Korenaga 2010; Zhang et al. 2012; Kane et al. 2019). Nonetheless, SO_2 does not constitute nearly as much of the Venusian atmosphere as one might expect, largely because it reacts with calcium carbonates to produce CO (Hong & Fegley 1997). Thus, one possible end state for a desiccated rocky planet’s atmosphere would be an atmosphere consisting of mainly CO_2 , N_2 , CO, CH_4 , and SO_2 . Any H_2O would remain through the moist greenhouse phase (if any), but would probably end up the same fate as past water on Venus: disassociation, loss of H_2 , and oxidization of the surface and reaction with CH_4 to produce more CO_2 (Kane et al. 2020).

4.1. Energy-limited Escape

We first estimate the atmospheric-loss rate from GJ 1252b using the formalism of energy-limited atmospheric escape (Salz et al. 2016), leaving more involved estimates of the planet’s mass-loss rate for future work. Using the MUSCLES treasury survey’s spectra of nearby M dwarfs (France et al. 2016; Loyd et al. 2016; Youngblood et al. 2016), we estimate an XUV flux incident on GJ 1252b of $(6\text{--}8) \times 10^3 \text{ erg s}^{-1} \text{ cm}^{-2}$. Assuming a heating efficiency of 0.3 (Salz et al. 2015) and that the planet’s optical transit radius is the same as its effective radius of XUV absorption, this XUV flux translates into an atmospheric mass-loss rate of roughly $0.1 M_{\oplus} \text{ Gyr}^{-1}$. The mass of a planet’s atmosphere is just $4\pi R_p^2 P_{\text{surf}} / g_{\text{surf}}$, which for GJ 1252b is $(5.3 \times 10^{18} \text{ kg})(P_{\text{surf}} / 1 \text{ bar})$. Thus, even a 100 bar atmosphere would be ablated in $<1 \text{ Myr}$. Note that, although GJ 1252

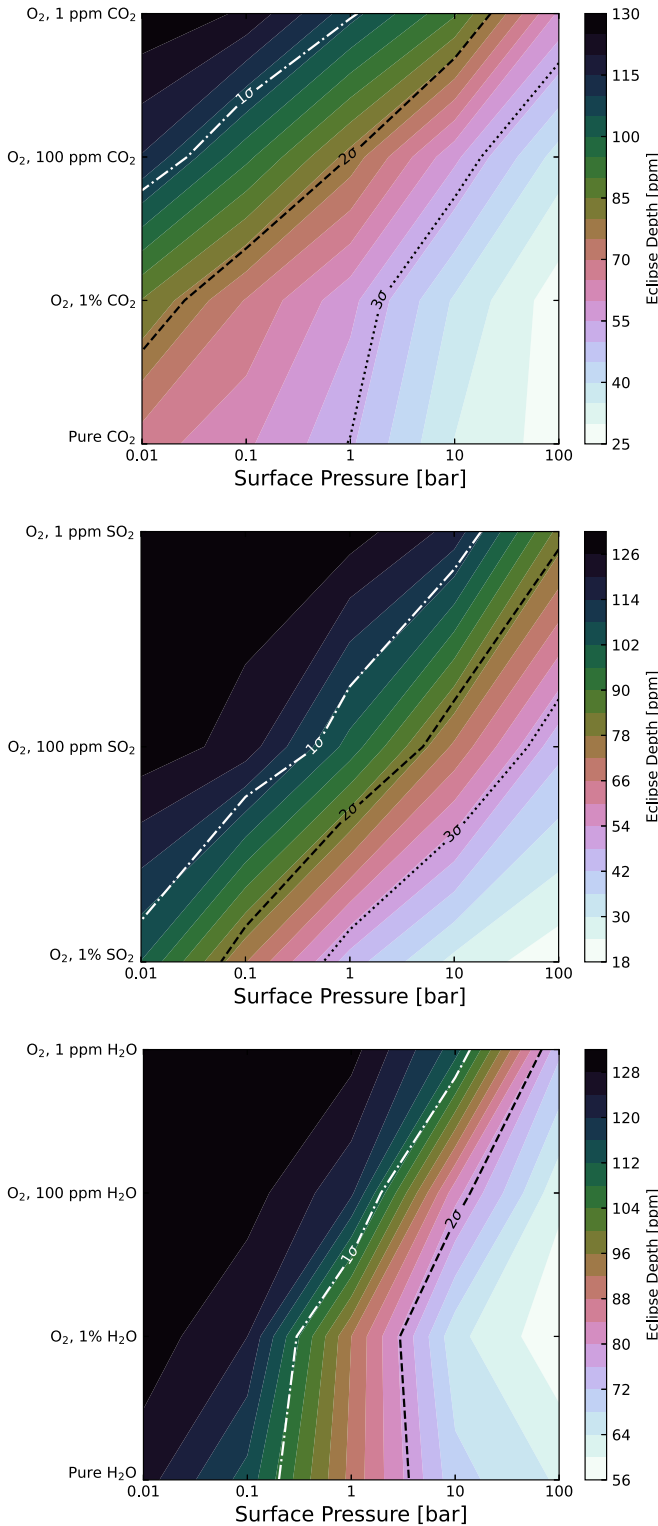


Figure 5. Same as Figure 4, but for atmospheres dominated by O_2 and with active IR absorbers of CO_2 (top), SO_2 (middle), and H_2O (bottom). Thick atmospheres ($P_{\text{surf}} \gtrsim 10$ bar) with mixing ratios of $\gtrsim 10^{-4}$ are disfavored in all cases.

exhibited no detectable stellar flares during its first sector of TESS observations (Howard 2022), the star was presumably more active, and thus mass-loss rates from GJ 1252b would have been even higher, earlier in the system’s lifetime.

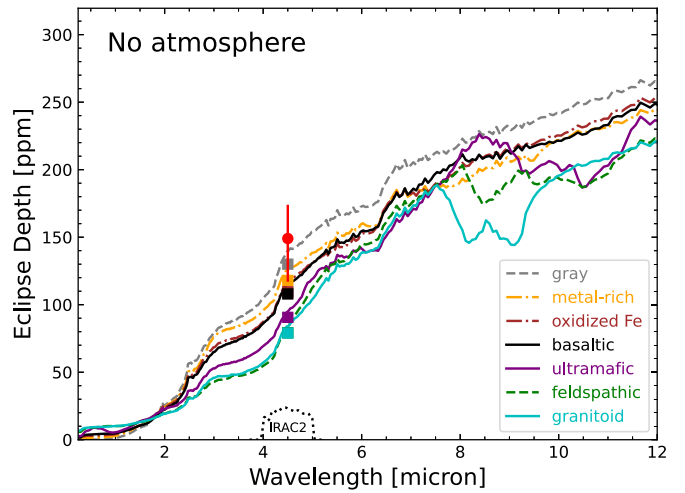


Figure 6. Simulated eclipse spectra of GJ 1252b from our suite of no-atmosphere models for different types of solid, unmelted surface mineralogies (lines; from Hu et al. 2012) compared to our measured depth and uncertainty (red circle with error bars). Squares show the values obtained by averaging the models over the IRAC2 bandpass (dotted line). All but the granitoid and feldspathic models are consistent with our measurement at $\leq 2\sigma$.

4.2. Comparing Outgassing and Escape Rates

To further evaluate the prospects for volatile loss from GJ 1252b, we modify the model of Foley & Smye (2018), Foley (2019) to apply to GJ 1252b and explore varying initial mantle CO_2 inventories that will still allow for a completely desiccated planet at the estimated planetary age of ~ 3.9 Gyr. Mantle gravity and core-radius-fraction model inputs were calculated using the mass–radius–composition solver, `ExoPlex` (Unterborn & Panero 2019). As the planet lacks any significant volatile atmosphere, we assumed the planet was made entirely of a FeO-free silicate mantle and pure-liquid-Fe core. Using a planet radius of $1.213 R_{\oplus}$ and a mass of $1.32 M_{\oplus}$, and assuming an Earth-like core radius fraction of 0.55%, `ExoPlex` calculates an average mantle density of 5026 kg m^{-3} and gravity 14.4 m s^{-2} . Due to the high surface temperature of the planet and the low likelihood of liquid water on the surface, we assume that the planet is in the stagnant lid regime of tectonics (as is, e.g., Venus; Gillmann et al. 2022). Our model then assumes all CO_2 outgassed from the mantle will accumulate in the atmosphere, as there is no known method of weathering or recycling carbon without water (Walker et al. 1981; Kasting & Catling 2003; Foley & Driscoll 2016). Our model also assumes an Earth-like heat-producing element budget, initial mantle temperature of 2000 K, and reference viscosity $\mu_{\text{ref}} = 1.3 \times 10^{20} \text{ Pa s}$ (Foley & Smye 2018).

Assuming an atmosphere mass-loss rate of $5 \times 10^6 \text{ kg s}^{-1}$, we vary the initial mantle CO_2 inventory of our model between an Earth-like initial inventory of 0.011 wt% (mass percentage), based on an estimate of 10^{22} mol of CO_2 in the mantle and surface reservoirs of Earth (Sleep & Zahnle 2001), to 7.3 wt% (over two orders of magnitude more CO_2 than on present-day Earth, by mass fraction).

Figure 7 shows the time evolution of total atmospheric pressure with varying initial mantle CO_2 inventories. For the larger carbon inventories considered, the planet’s initial rapid outgassing is greater than the atmospheric loss rate, allowing the atmospheric pressure to build before gradually being eroded once the mantle’s carbon store is depleted. However, for the Earth-like initial CO_2 (1.1×10^{-2} wt%), the atmospheric loss

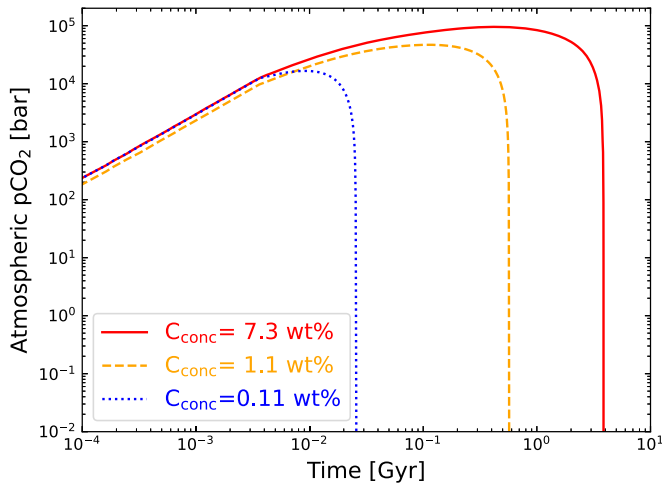


Figure 7. Time evolution of atmospheric pressure with variations in mantle carbon concentration (C_{conc}) for models assuming an otherwise Earth-like core. An Earth-like initial carbon concentration of 0.011 wt% (not shown) results in an atmospheric mass-loss rate always greater than the outgassing rate, so no atmosphere can build up. Models with greater carbon inventories than found on Earth build up temporary secondary atmospheres that are nonetheless lost within 4 Gyr. Even with orders of magnitude greater initial carbon inventory than Earth, GJ 1252b would have no significant remaining atmosphere, due to its prodigious atmospheric-loss rate.

rate is always greater than the outgassing rate and so the planet never builds a significant secondary atmosphere. All models tested result in a planet with a completely eroded atmosphere by 3.9 Gyr. Thus, GJ 1252b may have had orders of magnitude greater carbon inventory than Earth yet still have no remaining atmosphere today.

Taken together, our model spectra and escape calculations strongly indicate that GJ 1252b has no significant atmosphere.

5. Discussion and Conclusions

5.1. Comparisons with Similar Exoplanets

GJ 1252b joins the handful of small planets ($<2R_{\oplus}$) with infrared flux detections. The prior examples are 55 Cnc e (whose size and mass imply a sizable volatile mass fraction), LHS 3844b, and K2-141b;¹³ some relevant parameters for all these systems (including GJ 1252b) are listed in Table 3. GJ 1252b is smaller than all of these other planets, but intermediate in irradiation. We used the system parameters in Table 3, along with BT-Settl model stellar spectra (Allard 2014) interpolated to these stars’ parameters, to homogeneously calculate the irradiation and $4.5 \mu\text{m}$ dayside brightness temperatures of all these planets. The model spectra used for all four planets are included as machine-readable files with this paper.

As shown in Figure 8, a curious dichotomy emerges. The two smallest and coolest planets (GJ 1252b and LHS 3844b) both have dayside brightness temperatures ($T_{B,4.5 \mu\text{m}}$) consistent with the maximum possible dayside equilibrium temperature (i.e., $f = \frac{2}{3}$ and $A_B = 0$ in Equation (3)):

$$T_{\text{eq,max}} = \left(\frac{2}{3}\right)^{1/4} T_{\text{eff}} \sqrt{\frac{R_*}{a}}. \quad (4)$$

¹³ A similar measurement was also recently reported for TOI-824b (Roy et al., in press), but that planet’s bulk density clearly classifies it as a volatile-rich sub-Neptune rather than a rocky planet (Burt et al. 2020).

Table 3
Planets $< 2R_{\oplus}$ and with Measured Infrared Emission

Parameter	GJ 1252b ^a	LHS 3844b ^b	K2-141 b ^c	55 Cnc e ^d
R_p/R_{\oplus}	1.180	1.32	1.53	1.88
a/R_*	5.03	7.08	2.36	3.51
T_{eff}/K	3458	3036	4599	5172
$T_{\text{eq,max}}/\text{K}$	1390	1030	2705	2550
$\delta_{4.5 \mu\text{m}}/\text{ppm}$	149^{+25}_{-32}	380 ± 40	143 ± 39	83 ± 23^e
$T_{B,4.5 \mu\text{m}}/\text{K}$	1410^{+91}_{-125}	1011^{+32}_{-33}	2200^{+310}_{-330}	2040^{+270}_{-290}
$\text{ESM}_{7.5 \mu\text{m}}$	16.7	30.0	15.4	70.1 ^f

Notes.

^a From this work and Shporer et al. (2020).

^b From Vanderspek et al. (2019) and Kreidberg et al. (2019).

^c From Malavolta et al. (2018) and Zieba et al. (2022).

^d From Demory et al. (2016a) and Bourrier et al. (2018).

^e We adopt the standard deviation on the mean of the eclipse depths of Demory et al. (2016a) as a conservative estimate of this uncertainty. The weighted mean and its uncertainty from their first and second seasons of observations are 51 ± 17 ppm and 171 ± 27 ppm, respectively, corresponding to 1620 ± 230 K and 3070 ± 300 .

^f For stars as bright as 55 Cnc, ESM-like metrics typically overestimate the achievable S/N (Kempton et al. 2018).

On the other hand, the two largest and hottest planets (55 Cnc e and K2-141b) both have notably lower normalized dayside temperatures that are consistent with uniform heat redistribution ($f = \frac{1}{4}$).

This dichotomy may be coincidental: 55 Cnc e’s emission measurements are best interpreted as indicating a massive atmosphere, while the interpretation for K2-141b is a nonzero albedo but negligible atmosphere (Zieba et al. 2022). Some calculations predict that rocky planets with sufficiently intense irradiation could exhibit a high substellar albedo induced by photovolatilization of dayside rocky materials (Kite et al. 2016; Mansfield et al. 2019). One possibility is therefore that there is an irradiation threshold for this albedo enhancement, with GJ 1252b and LHS 3844b lying below it and K2-141b lying above it.

Alternatively, both 55 Cnc e and K2-141b may have atmospheres thick enough that they can transport sufficient heat to measurably cool their daysides. Evidence of 55 Cnc e’s thick atmosphere is seen in its asymmetric $4.5 \mu\text{m}$ phase curve (Demory et al. 2016b), but K2-141b’s $4.5 \mu\text{m}$ phase curve showed no such evidence for a thick atmosphere (Zieba et al. 2022)—this despite K2-141b’s dayside being heated high enough above the silicate solidus that an optically thick, ~ 0.1 bar mineral atmosphere is predicted. Future modeling and observations will both be needed in order to determine whether Figure 8 represents a coherent trend between some combination of irradiation, planet size, heat redistribution, and albedo.

Fortunately, GJ 1252 is bright enough to offer high S/N while faint enough to be observable with all of JWST’s instruments. With an Emission Spectroscopy Metric (ESM; Kempton et al. 2018) greater than K2-141b and within a factor of two of LHS 3844b (see Table 3), GJ 1252b is likely to join the select group of eminently observable and highly irradiated terrestrial exoplanets and to be subjected to many productive future investigations.

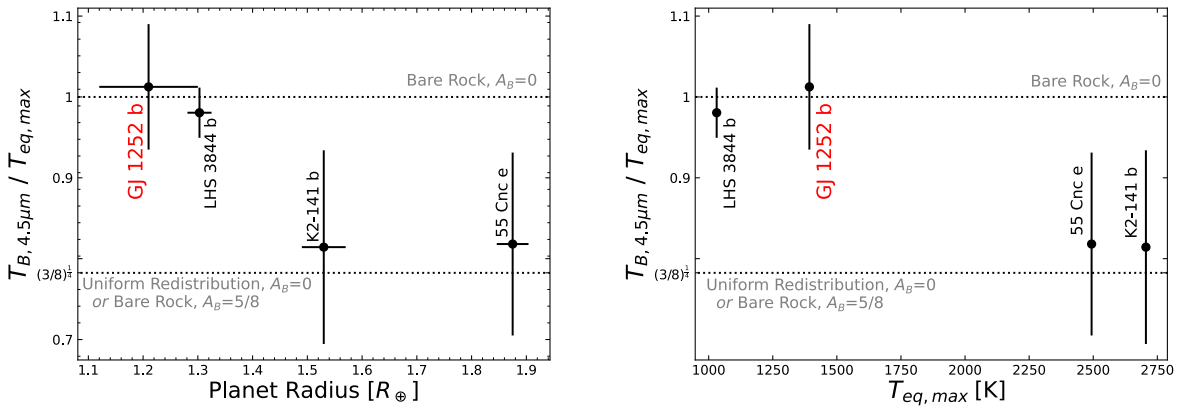


Figure 8. Normalized dayside brightness temperatures, $T_{B, 4.5 \mu\text{m}}$, of all super-Earths with infrared flux measurements plotted vs. planet radius (left) and $T_{\text{eq, max}}$ (right). The two smaller, cooler planets have $4.5 \mu\text{m}$ brightness temperatures consistent with no atmosphere and zero albedo, while the larger, hotter planets are significantly cooler and consistent with uniform redistribution of incident radiation and/or nonzero albedo.

(The data used to create this figure are available.)

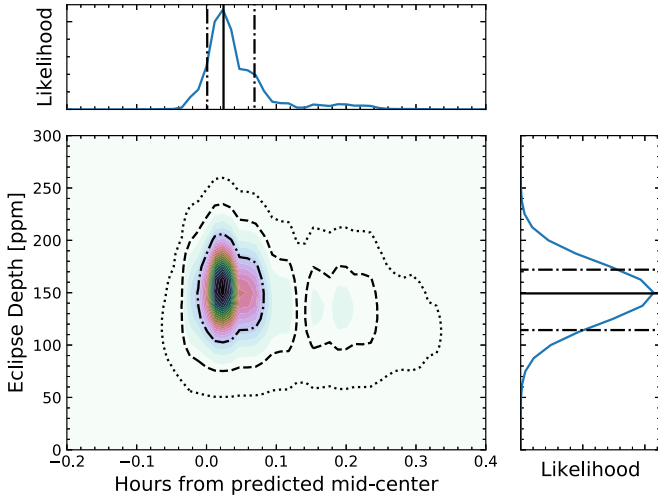


Figure 9. Joint posterior distributions of eclipse depth and time of eclipse center from the analysis plotted in Figure 2. The eclipse depth exhibits no covariance with the eclipse timing, despite the latter’s long tail toward high values.

5.2. Conclusions

We have presented our measurement of $4.5 \mu\text{m}$ thermal emission from the highly irradiated terrestrial planet GJ 1252b. With a radius of just $1.180 R_{\oplus}$, our target is the smallest planet for which such a measurement has been reported. After presenting our Spitzer data analysis, along with an updated transit analysis using new TESS data in Sections 2 and 3, we compared these measurements to a large suite of atmospheric models and simulated spectra. Our modeling demonstrated that, for a broad range of possible atmospheric compositions, surface pressures $P_{\text{surf}} \lesssim 10$ bar are required in order to be consistent with the measured eclipse at 2σ confidence. Furthermore, Section 4 then showed that the energy-limited atmospheric mass loss from GJ 1252b could quickly erode atmospheres with $P_{\text{surf}} > 100$ bar on timescales far shorter than the system lifetime.

We therefore conclude that GJ 1252b possesses no significant atmosphere. In this case, it presumably retains only a tenuous mineral exosphere; such an atmosphere would be expected to have $P_{\text{surf}} \lesssim 10^{-6}$ bar and to be dominated by

species such as Na, molecular O_2 and atomic O, and K (Miguel et al. 2011; Ito et al. 2015). Such an atmosphere is likely thin enough that atmospheric circulation would contribute negligibly to global heat and mass transfer (e.g., Nguyen et al. 2020), although detailed simulations will be needed to confirm this. Since GJ 1252b’s atmosphere would be quite optically thin, observations of GJ 1252b therefore offer the opportunity to directly probe surface mineralogy via emission spectroscopy during eclipse and throughout the planet’s orbit.

Infrared emission has been measured from only three exoplanets with sizes placing them firmly in the terrestrial planet regime. A larger sample is urgently needed in order to better identify the surface and atmospheric properties of this class of planets; fortunately, this number is already set to increase somewhat in the dawning JWST era (see discussion by Zieba et al. 2022). A further pressing need is to obtain more precise mass measurements for these planets: no mass has been reported for LHS 3844b, and GJ 1252b has only a roughly 3σ mass. The combination of more precise masses and bulk densities, more precise eclipse spectra, and stellar abundance measurements will ultimately enable more accurate models to link these planets’ surface mineralogies and atmospheres to their observed thermal emission.

We thank the anonymous referee for comments that substantively improved the quality of this work. We also thank Mike Werner, Katherine de Kleer, Daniel Koll, David Berardo, Courtney Dressing, and Farisa Morales for productive discussions about this project. We thank all the Spitzer Science Center staff for ensuring that these observations, as well as the Spitzer mission, were executed successfully. This work was supported in part by a grant from NASA’s Interdisciplinary Consortia for Astrobiology Research (ICAR). M.H. would like to acknowledge NASA support via the FINESST Planetary Science Division, NASA award number 80NSSC21K1536. Finally, I.J.M.C. thanks J.K.C. and N.L.C. for providing considerable logistical support while a large portion of the initial analysis was completed.

Facility TESS, Spitzer.

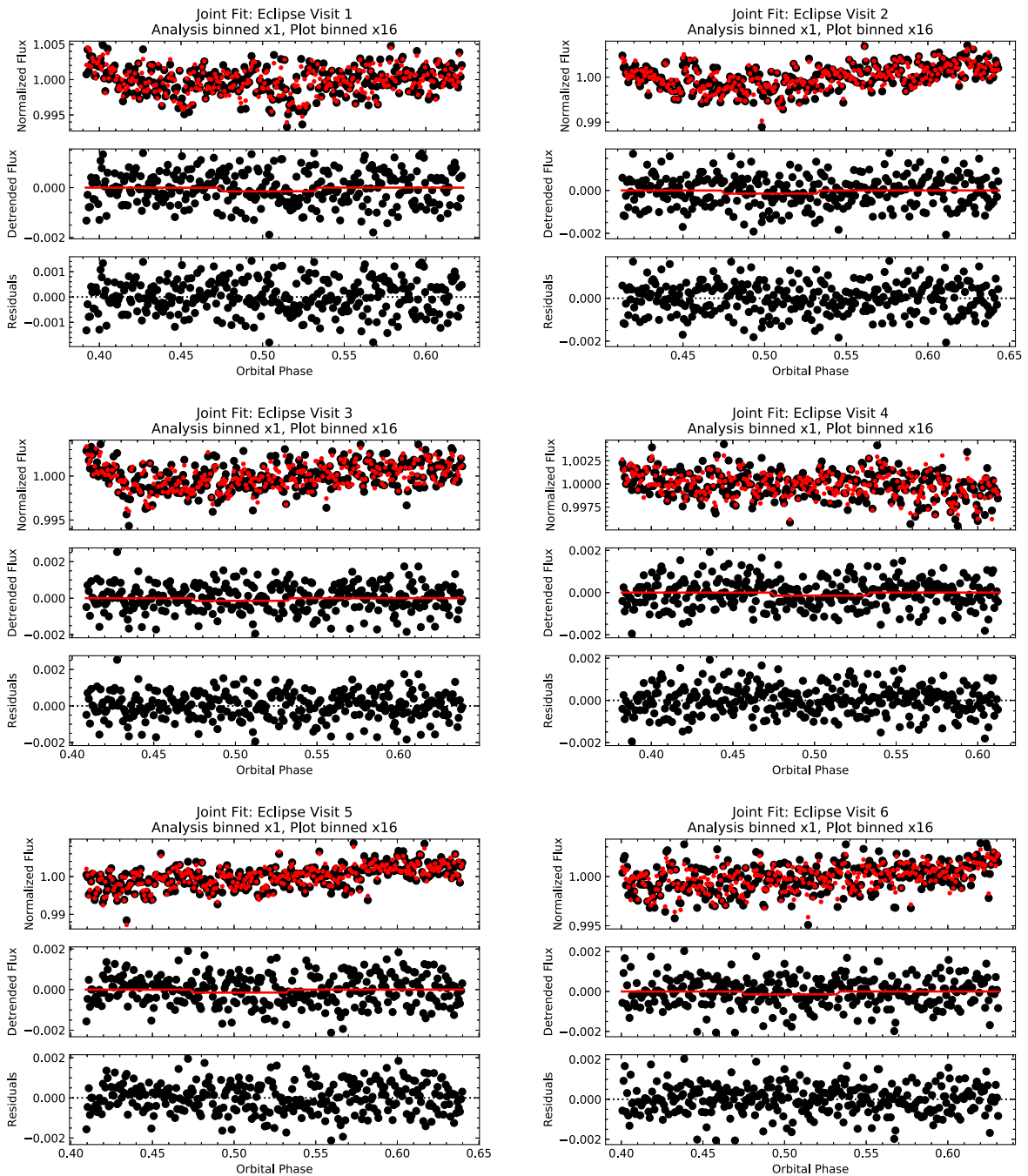


Figure 10. Spitzer 4.5 μm lightcurves for our joint analysis of all eclipse visits. In each triptych, the top panel shows the raw Spitzer photometry (black circles) vs. the PLD model (red points); the middle panel shows the systematics-corrected photometry (black circles) vs. the best-fit eclipse model (red line); the bottom panel shows the residuals. Although we performed our analysis without binning the data, the data are binned here by a factor of 16 for plotting purposes. Figure 2 shows the stacked average of all 10 eclipses.

Appendix

Figure 9 shows the joint posteriors on eclipse depth and time of eclipse for our primary, joint analysis. Figures 10 and 11 show the raw Spitzer photometry for each individual eclipse visit, the photometry after removal of systematics, and the residuals to the fits. Figure 12 shows how the residuals to these individual fits bin down with time.

ORCID iDs

Matej Malik <https://orcid.org/0000-0002-2110-6694>
Michelle L. Hill <https://orcid.org/0000-0002-0139-4756>

Stephen R. Kane <https://orcid.org/0000-0002-7084-0529>
Bradford Foley <https://orcid.org/0000-0002-6943-3192>
Alex S. Polanski <https://orcid.org/0000-0001-7047-8681>
Jonathan Brande <https://orcid.org/0000-0002-2072-6541>
Laura Kreidberg <https://orcid.org/0000-0003-0514-1147>
Nicolas B. Cowan <https://orcid.org/0000-0001-6129-5699>
Diana Dragomir <https://orcid.org/0000-0003-2313-467X>
Varoujan Gorjian <https://orcid.org/0000-0002-8990-2101>
Björn Benneke <https://orcid.org/0000-0001-5578-1498>
Jessie L. Christiansen <https://orcid.org/0000-0002-8035-4778>

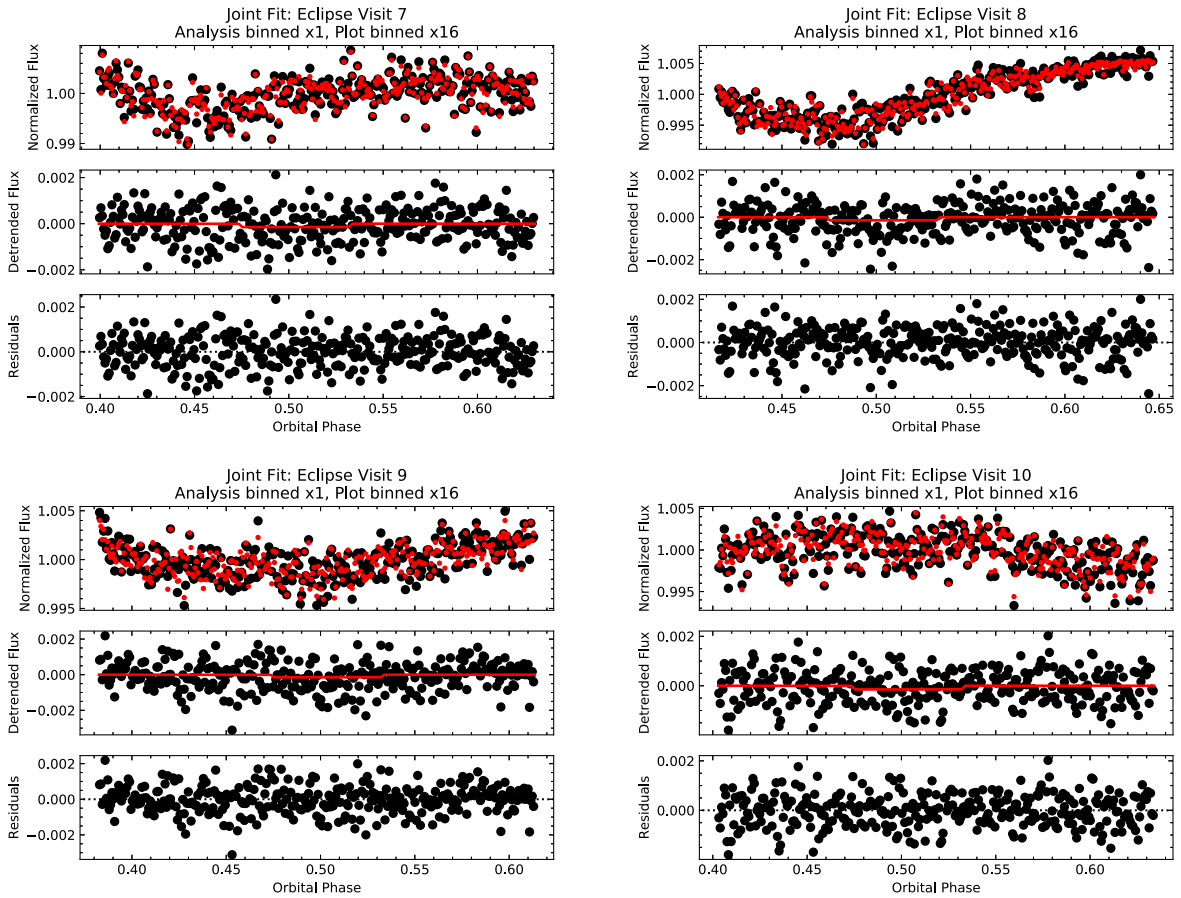


Figure 11. Same as Figure 10, but for the final four Spitzer eclipse visits.

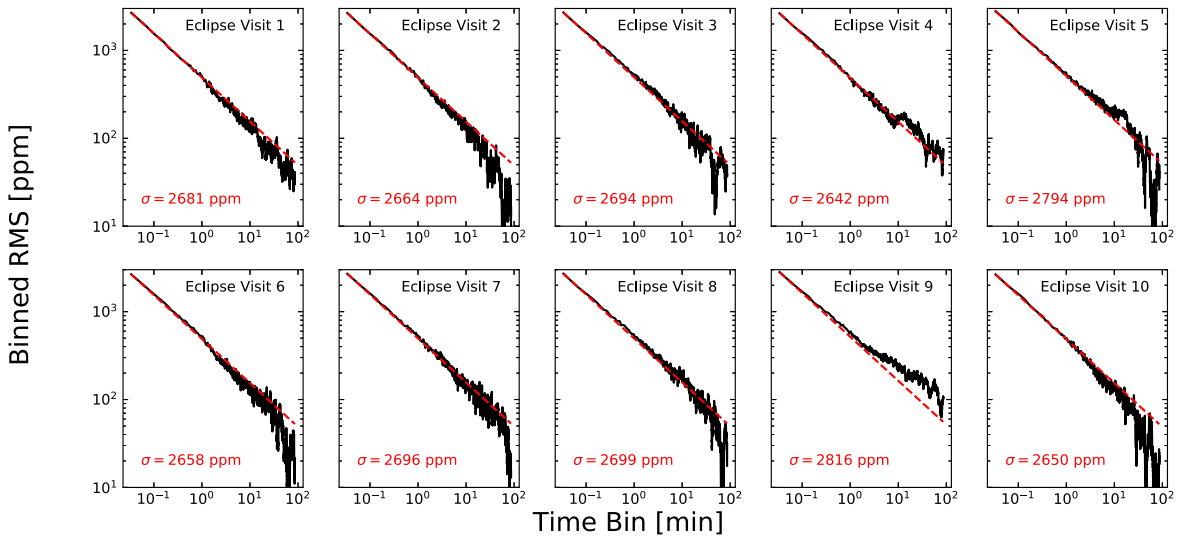


Figure 12. The dispersions of the binned residuals (solid black line) to the $4.5 \mu\text{m}$ lightcurves show limited evidence for correlated noise. The dashed lines show the expectations for wholly uncorrelated errors, which scale as $N^{-1/2}$.

References

Allard, F. 2014, in IAU Symp. 299, ed. M. Booth, B. C. Matthews, & J. R. Graham (Cambridge: Cambridge Univ. Press), 271
 Angelo, I., & Hu, R. 2017, *AJ*, 154, 232
 Batalha, N. M., Borucki, W. J., Bryson, S. T., et al. 2011, *ApJ*, 729, 27
 Bourrier, V., Dumusque, X., Dorn, C., et al. 2018, *A&A*, 619, A1
 Burrows, A., Budaj, J., & Hubeny, I. 2008, *ApJ*, 678, 1436
 Burt, J. A., Nielsen, L. D., Quinn, S. N., et al. 2020, *AJ*, 160, 153
 Claret, A. 2017, *A&A*, 600, A30

Cox, A. N. 2000, *Allen's Astrophysical Quantities* (New York: AIP Press)
 Crossfield, I., Werner, M., Dragomir, D., et al. 2018, *sptz prop*, 14084
 Crossfield, I. J. M., Petigura, E., Schlieder, J. E., et al. 2015, *ApJ*, 804, 10
 Crossfield, I. J. M., Ciardi, D. R., Petigura, E. A., et al. 2016, *ApJS*, 226, 7
 Dang, L., Calchi Novati, S., Carey, S., & Cowan, N. B. 2020, *MNRAS*, 497, 5309
 Deming, D., Knutson, H., Kammer, J., et al. 2015, *ApJ*, 805, 132
 Demory, B.-O., Gillon, M., Madhusudhan, N., & Queloz, D. 2016a, *MNRAS*, 455, 2018
 Demory, B.-O., Gillon, M., de Wit, J., et al. 2016b, *Natur*, 532, 207

- Engle, S. G., & Guinan, E. F. 2018, *RNAAS*, **2**, 34
- Esposito, L. W. 1984, *Sci*, **223**, 1072
- Essack, Z., Seager, S., & Pajusalu, M. 2020, *ApJ*, **898**, 160
- Fazio, G. G., Hora, J. L., Allen, L. E., et al. 2004, *ApJS*, **154**, 10
- Foley, B. J. 2019, *ApJ*, **875**, 72
- Foley, B. J., & Driscoll, P. E. 2016, *GGG*, **17**, 1885
- Foley, B. J., & Smye, A. J. 2018, *AsBio*, **18**, 873
- Foreman-Mackey, D., Luger, R., Agol, E., et al. 2021, *JOSS*, **62**, 3285
- France, K., Parke Loyd, R. O., Youngblood, A., et al. 2016, *ApJ*, **820**, 89
- Fulton, B. J., & Petigura, E. A. 2018, *AJ*, **156**, 264
- Gaillard, F., & Scaillet, B. 2014, *E&PSL*, **403**, 307
- Gillmann, C., Way, M. J., Avicé, G., et al. 2022, arXiv:2204.08540
- Goldblatt, C. 2015, *AsBio*, **15**, 362
- Gordon, I., Rothman, L., Hill, C., et al. 2017, *QJSTR*, **203**, 3
- Gordon, I., Rothman, L., Hargreaves, R., et al. 2022, *QJSTR*, **277**, 107949
- Grimm, S. L., & Heng, K. 2015, *ApJ*, **808**, 182
- Grimm, S. L., Malik, M., Kitzmann, D., et al. 2021, *ApJS*, **253**, 30
- Hammond, M., & Pierrehumbert, R. T. 2017, *ApJ*, **849**, 152
- Hansen, B. M. S. 2008, *ApJS*, **179**, 484
- Henning, W. G., O'Connell, R. J., & Sasselov, D. D. 2009, *ApJ*, **707**, 1000
- Hong, Y., & Fegley, B. 1997, *Icar*, **130**, 495
- Howard, W. S. 2022, *MNRAS*, **512**, L60
- Hu, R., Ehlmann, B. L., & Seager, S. 2012, *ApJ*, **752**, 7
- Ito, Y., Ikoma, M., Kawahara, H., et al. 2015, *ApJ*, **801**, 144
- Kane, S. R., Kopparapu, R. K., & Domagal-Goldman, S. D. 2014, *ApJL*, **794**, L5
- Kane, S. R., Roettenbacher, R. M., Unterborn, C. T., Foley, B. J., & Hill, M. L. 2020, *PSJ*, **1**, 36
- Kane, S. R., Arney, G., Crisp, D., et al. 2019, *JGRE*, **124**, 2015
- Kasting, J. F., & Catling, D. 2003, *ARA&A*, **41**, 429
- Kempton, E. M. R., Bean, J. L., Louie, D. R., et al. 2018, *PASP*, **130**, 114401
- Kite, E. S., Fegley, B. J., Schaefer, L., & Gaidos, E. 2016, *ApJ*, **828**, 80
- Koll, D. D. B. 2022, *ApJ*, **924**, 134
- Korenaga, J. 2010, *ApJL*, **725**, L43
- Kreidberg, L., Koll, D. D. B., Morley, C., et al. 2019, *Natur*, **573**, 87
- Lammer, H., Sproß, L., Grenfell, J. L., et al. 2019, *AsBio*, **19**, 927
- Li, G., Gordon, I. E., Rothman, L. S., et al. 2015, *ApJS*, **216**, 15
- Lightkurve Collaboration, Cardoso, J. V. D. M., Hedges, C., et al. 2018, Lightkurve: Kepler and TESS Time Series Analysis in Python, Astrophysics Source Code Library, ascl:1812.013
- Lloyd, R. O. P., France, K., Youngblood, A., et al. 2016, *ApJ*, **824**, 102
- Luger, R., & Barnes, R. 2015, *AsBio*, **15**, 119
- Madhusudhan, N. 2012, *ApJ*, **758**, 36
- Malavolta, L., Mayo, A. W., Loudon, T., et al. 2018, *AJ*, **155**, 107
- Malik, M., Kempton, E. M. R., Koll, D. D. B., et al. 2019a, *ApJ*, **886**, 142
- Malik, M., Kitzmann, D., Mendonça, J. M., et al. 2019b, *AJ*, **157**, 170
- Malik, M., Grosheintz, L., Mendonça, J. M., et al. 2017, *AJ*, **153**, 56
- Mandel, K., & Agol, E. 2002, *ApJL*, **580**, L171
- Mansfield, M., Kite, E. S., Hu, R., et al. 2019, *ApJ*, **886**, 141
- Miguel, Y., Kaltenecker, L., Fegley, B., & Schaefer, L. 2011, *ApJL*, **742**, L19
- Millholland, S., & Laughlin, G. 2019, *NatAs*, **3**, 424
- Modirrousta-Galian, D., Ito, Y., & Micela, G. 2021, *Icar*, **358**, 114175
- Nguyen, T. G., Cowan, N. B., Banerjee, A., & Moores, J. E. 2020, *MNRAS*, **499**, 4605
- Polyansky, O. L., Kyuberis, A. A., Zobov, N. F., et al. 2018, *MNRAS*, **480**, 2597
- Richard, C., Gordon, I. E., Rothman, L. S., et al. 2012, *QJSTR*, **113**, 1276
- Rothman, L., Gordon, I., Barber, R., et al. 2010, *QJSTR*, **111**, 2139
- Salz, M., Schneider, P. C., Czesla, S., & Schmitt, J. H. M. M. 2015, *A&A*, **576**, A42
- Salz, M., Schneider, P. C., Czesla, S., & Schmitt, J. H. M. M. 2016, *A&A*, **585**, L2
- Savitzky, A., & Golay, M. J. E. 1964, *AnaCh*, **36**, 1627
- Schaefer, L., Wordsworth, R. D., Berta-Thompson, Z., & Sasselov, D. 2016, *ApJ*, **829**, 63
- Seager, S. 2010, *Exoplanet Atmospheres: Physical Processes* (Princeton, NJ: Princeton Univ. Press)
- Sheets, H. A., & Deming, D. 2014, *ApJ*, **794**, 133
- Shporer, A., Collins, K. A., Astudillo-Defru, N., et al. 2020, *ApJL*, **890**, L7
- Sleep, N. H., & Zahnle, K. 2001, *JGR*, **106**, 1373
- Sneep, M., & Ubachs, W. 2005, *QJSTR*, **92**, 293
- Stassun, K. G., Oelkers, R. J., Pepper, J., et al. 2018, *AJ*, **156**, 102
- Tamburo, P., Mandell, A., Deming, D., & Garhart, E. 2018, *AJ*, **155**, 221
- Thalman, R. J., Zarzana, K., Tolbert, M., & Volkamer, R. 2014, *QJSTR*, **147**, 171
- Underwood, D. S., Tennyson, J., Yurchenko, S. N., et al. 2016, *MNRAS*, **459**, 3890
- Unterborn, C. T., & Panero, W. R. 2019, *JGRE*, **124**, 1704
- Vanderspek, R., Huang, C. X., Vanderburg, A., et al. 2019, *ApJ*, **871**, L24
- Wagner, W., & Kretzschmar, H.-J. 2008, *International Steam Tables—Properties of Water and Steam Based on the Industrial Formulation IAPWS-IF97* (Berlin, Heidelberg: Springer)
- Walker, J. C. G., Hays, P. B., & Kasting, J. F. 1981, *JGR*, **86**, 9776
- Winn, J. N. 2010, arXiv:1001.2010
- Wordsworth, R., & Kreidberg, L. 2021, arXiv:2112.04663
- Wordsworth, R., & Pierrehumbert, R. 2014, *ApJL*, **785**, L20
- Youngblood, A., France, K., Loyd, R. O. P., et al. 2016, *ApJ*, **824**, 101
- Yurchenko, S. N., Amundsen, D. S., Tennyson, J., & Waldmann, I. P. 2017, *A&A*, **605**, A95
- Zahnle, K. J., & Catling, D. C. 2017, *ApJ*, **843**, 122
- Zhang, X., Liang, M. C., Mills, F. P., Belyaev, D. A., & Yung, Y. L. 2012, *Icar*, **217**, 714
- Zieba, S., Zilinskas, M., Kreidberg, L., et al. 2022, *A&A*, **664**, A79